



One-pot solvothermal synthesis of MoS₂-modified Mn_{0.2}Cd_{0.8}S/MnS heterojunction photocatalysts for highly efficient visible-light-driven H₂ production

Jinming Wang¹, Jiang Luo¹, Dong Liu, Shengtao Chen, Tianyou Peng*

College of Chemistry and Molecular Sciences, Wuhan University, Wuhan 430072, PR China

ARTICLE INFO

Keywords:

MnxCd_{1-x}S solid solution
Heterojunction
Nanorod
MoS₂ cocatalyst
Hydrogen evolution

ABSTRACT

Development of low-cost, highly efficient and stable CdS-based solid solution photocatalysts is of great significance towards photocatalytic H₂ production. Herein, a solvothermal process has been used to fabricate Mn_xCd_{1-x}S-based products, which can transform into novel heterojunctions consisting of nanorod-like Mn_{0.2}Cd_{0.8}S solid solution and nanoparticle-like α-MnS once the *x* value is higher than 0.20, and the resulted Mn_{0.2}Cd_{0.8}S/MnS heterojunction containing 38 mol% α-MnS demonstrates an optimum composition ratio with the best H₂ production activity (335 μmol h⁻¹), which is 1.95 times higher than that (171 μmol h⁻¹) of the single CdS under visible light (λ ≥ 420 nm) irradiation. After modified with MoS₂ cocatalyst *via* a one-pot solvothermal process, those MoS₂-Mn_{0.2}Cd_{0.8}S/MnS composites show significantly improved photocatalytic performance, and the 15 wt% MoS₂-Mn_{0.2}Cd_{0.8}S/MnS achieves the best H₂ production activity (995 μmol h⁻¹), which is 2.97 times higher than that (335 μmol h⁻¹) of the pristine Mn_{0.2}Cd_{0.8}S/MnS with the optimum composition ratio and also higher than that (868 μmol h⁻¹) of the 1.0 wt% Pt-Mn_{0.2}Cd_{0.8}S/MnS. The well aligned energy band structures and the intimate contacts among Mn_{0.2}Cd_{0.8}S, α-MnS and MoS₂ facilitate the photogenerated electron transferring from the nanoparticle-like α-MnS to the nanorod-like Mn_{0.2}Cd_{0.8}S and then to the nanoflake-like MoS₂, thus promoting the charge separation and providing more active sites for H₂ production reaction. This study not only presents a rare example of binary Mn_{0.2}Cd_{0.8}S/MnS heterojunction photocatalyst consisting of Mn_{0.2}Cd_{0.8}S solid solution and α-MnS, but also paves a new way to explore highly efficient and noble metal-free photocatalytic H₂ production system for solar energy conversion.

1. Introduction

Since the photosplitting water over TiO₂ electrode was reported for the first time in 1972 [1], various semiconducting materials have been developed for photocatalytic H₂ production since it has been thought as one of the promising solutions to the growing energy crisis and global warming [2,3]. As one of the most extensively investigated photocatalysts, TiO₂ only absorbs UV light of the solar spectrum due to its wide band gap (~3.20 eV), while the solar energy (AM1.5G) contains only ~4% UV rays with wavelengths shorter than 400 nm, ~53% visible light with wavelengths in the range of 400–800 nm, and ~43% infrared rays with wavelengths longer than 800 nm [4]. Therefore, various strategies have been developed to exploit more ideal photocatalysts that are capable of utilizing low energy photons in visible regions so as to maximize its use of naturally available sunlight and

make the photocatalytic reactions more efficient [5–9].

As visible-light-responsive semiconductors, certain metal sulfides with adjustable energy band structures have been extensively investigated in the field of photocatalysis [10–18]. Among them, CdS has attracted tremendous attentions due to its narrow band gap (~2.40 eV) and good visible-light-driven H₂ production activity [14–18], but the principal barriers to its large-scale application are severe photocorrosion and fast charge recombination [2–4]. Therefore, various approaches such as constructing heterojunctions or nanocomposites [14–16], modifying with co-catalysts [16–18], and fabricating multi-component solid solutions [19–23], have been adopted to further improve the photocatalytic activity and stability of those CdS-based photocatalysts. Among which, the multi-component solid solutions usually exhibit better activity than the single CdS since their band gaps can be easily tuned by varying the composition ratios to meet the

* Corresponding author.

E-mail address: typeng@whu.edu.cn (T. Peng).

¹ These authors contributed to this work equally.

requirement of water splitting reactions [24]. Nevertheless, a number of CdS-based photocatalysts are still less than the metal oxide-based ones in stability that was the most serious disadvantage of the CdS-based photocatalysts [25–28]. In 2010, $\text{Mn}_{1-x}\text{Cd}_x\text{S}$ ($x \sim 0.1$) solid solution with highly efficient H_2 production activity and excellent tolerance to photocorrosion was reported for the first time [25]. Thereafter, various strategies such as doping with transition metal [29], constructing heterojunction [30], or cocatalyst modification [31–34], have been employed to further upgrade the activity and stability of $\text{Mn}_{1-x}\text{Cd}_x\text{S}$. Although noble metal Pt is widely used as cocatalyst for promoting the H_2 production reaction, the scarcity and high cost limited its large-scale application [2–4]. Therefore, to develop efficient, stable and earth-abundant cocatalyst is of significance towards improving the activity and stability of $\text{Cd}_x\text{Mn}_{1-x}\text{S}$ solid solutions [33,34].

In the past decades, MoS_2 has been used as highly efficient and low-cost cocatalyst [34–38]. Zong and co-workers [35] reported that MoS_2 on CdS achieved better H_2 production activity than certain noble metals. Similarly, MoS_2 thin layers loaded on mesoporous graphitic carbon nitride (mpg-CN) significantly improved the visible-light-driven H_2 production activity [36]. Those MoS_2 cocatalysts not only serve as electron sink to retard the charge recombination, but also offer accessible reactive sites to promote H_2 production activity of CdS [39–45]. Also, the strong interfacial contact between MoS_2 and CdS is essential for efficient charge migration from semiconductor to MoS_2 [35]. More recently, it was reported that the introduction of MoS_2 led to a remarkable improvement in H_2 production activity of $\text{Mn}_{0.25}\text{Cd}_{0.75}\text{S}$ [34]. As far as we know, it is a rare sample of using MoS_2 as cocatalyst of $\text{Mn}_x\text{Cd}_{1-x}\text{S}$ solid solution to promote the charge separation and offer more active sites for H_2 generation.

Herein, a series of MoS_2 -modified $\text{Mn}_x\text{Cd}_{1-x}\text{S}$ -based products have been successfully fabricated via a facile one-pot solvothermal process. It was found that the $\text{Mn}_x\text{Cd}_{1-x}\text{S}$ -based products can transform into novel $\text{Mn}_{0.2}\text{Cd}_{0.8}\text{S}/\text{MnS}$ heterojunctions consisting of nanorod-like $\text{Mn}_{0.2}\text{Cd}_{0.8}\text{S}$ solid solution and nanoparticle-like α -MnS by increasing the x value from 0.20 to 0.75, and the resulted $\text{Mn}_{0.2}\text{Cd}_{0.8}\text{S}/\text{MnS}$ heterojunction containing 38 mol% α -MnS demonstrates an optimum composition ratio with a much better H_2 production activity than that of the single CdS under visible light ($\lambda \geq 420$ nm) irradiation. Moreover, MoS_2 modification results in significantly improved photocatalytic performance that exceeds the noble metal Pt towards photocatalytic H_2 production. Based on the experimental results and material characterizations, a possible mechanism of the enhanced photocatalytic activity of MoS_2 -modified $\text{Mn}_{0.2}\text{Cd}_{0.8}\text{S}/\text{MnS}$ was proposed.

2. Experimental

2.1. Material preparation

$\text{Mn}_x\text{Cd}_{1-x}\text{S}$ -based products were synthesized through a solvothermal process. Typically, a mixture of thiourea ($\text{SC}(\text{NH}_2)_2$, 6.0 mmol), Cd(Ac) $_2$ ·4 H_2O and Mn(Ac) $_2$ ·2 H_2O with appropriate amounts was dissolved in ethylenediamine (60 mL) under magnetically stirring for 15 min, and then the mixed solution was transferred into a Teflon-lined stainless-steel autoclave (100 mL) for heat treating at 160 °C for 24 h. After cooling naturally, the precipitate was centrifuged, washed with water and ethanol several times, and then dried in a vacuum oven at 70 °C overnight to obtain the $\text{Mn}_x\text{Cd}_{1-x}\text{S}$ -based product. By varying the addition amounts of Cd(Ac) $_2$ and Mn(Ac) $_2$, a series of $\text{Mn}_x\text{Cd}_{1-x}\text{S}$ -based products with different x values were obtained according to the same procedures.

MoS_2 -modified $\text{Mn}_{0.2}\text{Cd}_{0.8}\text{S}/\text{MnS}$ heterojunction with 38 mol% α -MnS was synthesized through a one-pot solvothermal process similar to the procedure mentioned above. Typically, a mixture of Cd(Ac) $_2$ ·4 H_2O (1.0 mmol), Mn(Ac) $_2$ ·2 H_2O (1.0 mmol), $\text{SC}(\text{NH}_2)_2$ (6.0 mmol) and Na_2MoO_4 ·2 H_2O with appropriate amount was dissolved in ethylenediamine (60 mL) under magnetically stirring for 15 min, then the mixed

solution was transferred into a Teflon-lined stainless-steel autoclave (100 mL) for heat treating at 160 °C for 24 h. After cooling naturally, the precipitate was centrifuged, washed with water and ethanol several times, and then dried in a vacuum oven at 70 °C overnight to obtain the MoS_2 -modified $\text{Mn}_{0.2}\text{Cd}_{0.8}\text{S}/\text{MnS}$ heterojunctions. For comparison, Pt as co-catalyst was also deposited on the $\text{Mn}_{0.2}\text{Cd}_{0.8}\text{S}/\text{MnS}$ heterojunction with 38 mol% α -MnS via a photoreduction reaction process [8,9]. Typically, $\text{Mn}_x\text{Cd}_{1-x}\text{S}$ -based product (0.20 g) was dispersed in 100 mL of methanol aqueous solution (20 vol% methanol) containing H_2PtCl_6 solution (0.077 M) with an ultrasonic bath for 30 min, which was irradiated by a 500 W high pressure Hg-lamp for 3 h under magnetically stirring. 1.0 wt% Pt-loaded $\text{Mn}_{0.2}\text{Cd}_{0.8}\text{S}/\text{MnS}$ heterojunction was obtained by centrifugation, washed with water and ethanol several times, and then dried in a vacuum oven at 80 °C overnight.

2.2. Material characterization

The crystal phases analyses were carried out using a Rigaku Miniflex 600 X-ray diffractometer (XRD) with Cu K α 1 radiation ($\lambda = 0.154178$ nm) at 40 kV, 40 mA and a scan rate of 6° min $^{-1}$ in the range of $2\theta = 10^\circ$ – 70° . Elemental compositions of the obtained products were detected using a Bruker S4 Pioneer X-ray fluorescence (XRF) spectrometer with a Rh target and without standard sample. The α -MnS contents in those $\text{Mn}_x\text{Cd}_{1-x}\text{S}$ -based products were analyzed quantitatively with K value method by XRD technique [46], whereby a mixture of α - Al_2O_3 powder (as a reference) and home-made α -MnS with 1:1 mass ratio was used to measure the K value, which is equal to the XRD peak intensity (I) ratio of α - Al_2O_3 and α -MnS in the mixture [$K = I(\alpha\text{-Al}_2\text{O}_3)/I(\alpha\text{-MnS})$]. After that, a mixture of α - Al_2O_3 and $\text{Mn}_x\text{Cd}_{1-x}\text{S}$ -based product with 1:4 mass ratio was used to the XRD measurement, and the α -MnS content in those $\text{Mn}_x\text{Cd}_{1-x}\text{S}$ -based products was calculated according to the following equation:

$$w_i = K \times \frac{I_i \times w_s}{I_s \times (1 - w_s)}$$

where w_i is the mass ratio of α -MnS in the mixture (α - Al_2O_3 + $\text{Mn}_x\text{Cd}_{1-x}\text{S}$ -based product); I_i is the XRD peak intensity of α -MnS in the mixture; I_s is the XRD peak intensity of the added α - Al_2O_3 in the mixture; w_s is the mass ratio of α - Al_2O_3 (20%) in the mixture.

The morphology was observed using Zeiss-Sigma field emission scanning electron microscope (FESEM). High-resolution transmission electron microscopy (HRTEM) was performed at 200 kV on a field-emission electron microscope (JEM2100(HR)) with an ultrahigh-resolution pole piece. The element mappings of samples were obtained using FEI Tecnai G2 F30 transmission electron microscopy equipped with energy dispersive X-ray spectrometric microanalysis (EDX) unit. UV–vis diffuse reflectance absorption spectra (DRS) were recorded at ambient temperature on a Shimadzu MPC-3100 with BaSO $_4$ as the reference sample under scanning scope from 300 to 900 nm. X-ray photoelectron spectra (XPS) were determined using Thermo Fisher ESCALAB 250Xi X-ray photoelectron spectroscopy equipped with a standard and monochromatic source (Al K α) operated at 300 W and calibrated with C 1s. Photoluminescence (PL) spectra were carried out on a Hitachi Model F-6800 fluorescence spectrophotometer. Liquid N $_2$ adsorption-desorption isotherms at 77 K were measured by a Micromeritics ASAP 2010 system.

Transient photocurrent curves and electrochemical impedance spectra (EIS) were obtained by using a CHI Model 618C electrochemical analyzer and a standard three-electrode system, in which Pt wire, Pt plate, and saturated calomel electrode (SCE) acted as the work, counter, and reference electrode, respectively. The work electrode was prepared by depositing catalyst Nafion suspension solution (200 μL , 4.0 g L $^{-1}$) on the fluorine-tin-oxide-coated glass (1 cm 2), which was heated at 70 °C for 1 h to volatilize the solvent and steady the catalyst. In a typical run, the three electrodes were immersed into a suspension containing Na $_2\text{SO}_4$ solution (1.0 M) and 3.0 mg methyl viologen (MV) as electron

media, which was continuously purged by N₂ flow for 30 min before light irradiation.

For the measurement of flat-band potential (E_{fb}), the film electrode was prepared on clean fluorine-doped tin oxide (FTO) glass as follows: the as-prepared sample (10 mg) was uniformly mixed with a mixed solvent (0.5 mL) containing alcohol, α -terpineol and hydroxyethyl cellulose under grind and sonication for 60 min, and then the resultant paste was spread onto a 1.0 cm² FTO glass. After air-drying and calcination at 300 °C for 1 h in Ar atmosphere, the obtained film electrode was used as working electrode for the electrochemical testing in Na₂SO₄ solution (1.0 M) with various frequencies by using Ag/AgCl (saturated KCl solution) as reference electrode and Pt foil as the counter electrode, and then the E_{fb} value was determined by the Mott-Schottky relation [12].

2.3. Photocatalytic property tests

The photocatalytic H₂ production reaction was carried out in a sealed top-irradiation reaction vessel (Pyrex glass). A total of photocatalyst (0.05 g) was suspended in an aqueous solution (50 mL) containing Na₂S (0.35 M) and Na₂SO₃ (0.25 M) as sacrificial electron donors. Visible light ($\lambda \geq 420$ nm) irradiation was obtained using a 300 W Xe-lamp combined with a UV-cutoff filter. Before irradiation, the air in the photoreaction system should be removed completely, and the H₂ production amount was determined using a gas chromatograph (GC, SP6980, TCD detector, 5 Å molecular sieve columns and Ar carrier). Monochromatic light used in the measurement of apparent quantum yield (AQY) was acquired by inserting an appropriate band-pass filter ahead of the 300 W Xe-lamp to obtain the correct monochromatic light, and its intensity was determined by using a SRC-1000-TC-QZ-N monocrystalline silicon cell (Oriel, USA). AQY values were calculated according to the following equation.

$$AQY(\%) = \frac{\text{number of reacted electrons}}{\text{number of incident photons}} \times 100$$

3. Results and discussion

3.1. Crystal phase and composition analyses

Fig. 1 depicts the XRD patterns of various Mn_xCd_{1-x}S-based products ($0 \leq x \leq 1.0$) derived from the solvothermal treatment at 160 °C. As can be seen from Fig. 1a, the XRD profile of the Mn_xCd_{1-x}S-based product with $x = 0$ (the single CdS) exhibits characteristic peaks at $2\theta = 24.8^\circ, 26.3^\circ, 28.2^\circ, 36.6^\circ, 43.7^\circ, 47.8^\circ$ and 51.8° , ascribable to the reflections of (100), (002), (101), (102), (110), (103) and (112) planes of hexagonal CdS (JCPDS No. 41-1049) [44], respectively. No other

crystalline impurity can be detected from the XRD pattern of the single CdS, indicating that hexagonal CdS with high crystal phase purity can be formed during the present solvothermal process. Whereas, the XRD pattern of the Mn_xCd_{1-x}S-based product with $x = 1.0$ (the single MnS) has diffraction peaks located at $2\theta = 29.6^\circ, 34.3^\circ, 49.3^\circ$ and 61.4° , which can be indexed to the reflections of (111), (200), (220) and (222) planes of rock salt-typed cubic α -MnS (JCPDS No. 06-0518) [34], respectively. It indicates that the present solvothermal treatment leads to the formation of thermodynamically stable α -MnS, which is reasonable by considering that the unstable phase such as β -MnS and γ -MnS can be readily transformed into α -MnS at the high temperature or pressure [25,29,34].

Along with increasing x value from 0 to 0.15 and 0.20, the (100), (002) and (101) diffraction peaks of Mn_xCd_{1-x}S-based products slightly shift towards higher diffraction angles accompanied by decreased intensities compared to the hexagonal CdS (Fig. 1b). This successive shifts in the diffraction peaks along with the x value enhancing from 0 to 0.20 demonstrate that these products are Mn_xCd_{1-x}S solid solution but not a MnS/CdS mixture since Mn²⁺ ions with radii (0.46 Å) smaller than Cd²⁺ (0.97 Å) can incorporate into the CdS lattice or its interstitial sites [34,44]. Nevertheless, there is no further shift in those diffraction peaks upon further increasing x value from 0.20 to 0.75 (Fig. 1b). It implies that α -MnS has very limited solubility in the CdS lattice to form Mn_{0.2}Cd_{0.8}S solid solution during the present solvothermal process, which leads to the preferential formation of thermodynamically stable α -MnS once the x value is higher than 0.20. Upon enhancing the x value from 0.25 to 0.75, those newly appeared diffraction peaks at $2\theta = 34.3^\circ, 49.3^\circ$ and 61.4° , ascribable to the (200), (220) and (222) planes of α -MnS, exhibit an increasing trend (Fig. 1a). The above results demonstrate that α -MnS coexists in those Mn_xCd_{1-x}S-based products with x higher than 0.20 [34,44], which might form heterojunctions consisting of Cd_{0.8}Mn_{0.2}S solid solution and α -MnS.

To confirm the above conjecture, the element compositions of those Mn_xCd_{1-x}S-based products ($0 \leq x \leq 1.0$) were determined using XRF technique, and the relative molar percentages of Mn, Cd and S in the products are listed in Table 1. As seen, the Mn:Cd:S molar ratios in those products are very similar to that of their respective addition amounts during the preparation process. Also, the α -MnS contents in those Mn_xCd_{1-x}S-based products were analyzed quantitatively with K value method by XRD technique [46], and the corresponding molar percentages of α -MnS are also listed in Table 1. As can be seen, Mn_xCd_{1-x}S-based products begin to contain α -MnS once x value is higher than 0.20, and its molar percentage shows an increasing trend along with further enhancing the x value. After excluding the α -MnS percentages in those Mn_xCd_{1-x}S-based products with x higher than 0.20, the calculated solid solution compositions show a similar molar ratio of Mn:Cd:S = 0.2:0.8:1 (Table 1). These results indicate that the

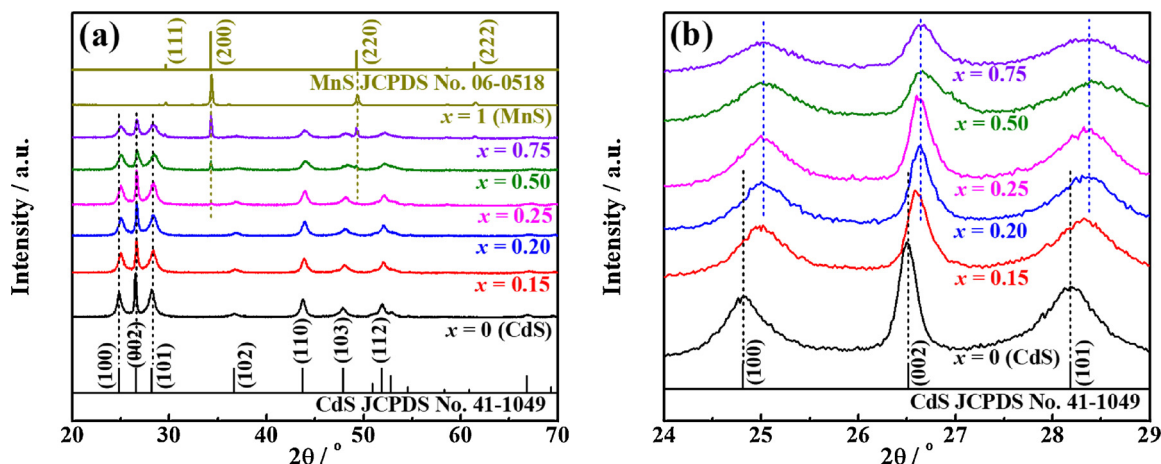


Fig. 1. (a) XRD patterns of the Mn_xCd_{1-x}S-based products with different x values. (b) XRD patterns at the lower angle region ($24^\circ < 2\theta < 29^\circ$) of figure (a).

Table 1
Composition ratios, band gaps of $\text{Mn}_x\text{Cd}_{1-x}\text{S}$ -based products with different x values.

x value	$\text{Mn}_x\text{Cd}_{1-x}\text{S}^{\text{a}}$			Mn:Cd:S molar ratio ^b	$\alpha\text{-MnS}^{\text{c}}$ /mol%	Solid solution nanorod ^d			Mn:Cd:S molar ratio ^d
	Mn/mol%	Cd/mol%	S/mol%			Mn/mol%	Cd/mol%	S/mol%	
0	0	49.7	50.3	0:0.99:1	0	–	–	–	–
0.15	7.8	42.5	49.7	0.16:0.85:1	0	–	–	–	–
0.20	9.5	40.3	50.2	0.19:0.81:1	0	–	–	–	–
0.25	11.5	38.7	49.8	0.23:0.78:1	5.7	10.2	39.8	50	0.20:0.80:1
0.50	24.5	25.4	50.1	0.49:0.51:1	38	9.6	40.4	50	0.19:0.81:1
0.75	36.5	13.5	50.0	0.73:0.27:1	69	9.8	40.2	50	0.20:0.80:1
1.0	49.4	0	50.6	0.98:0:1	100	–	–	–	–

^a Measured using XRF technique.

^b Calculated according to the XRF analytical results.

^c Measured using K value method by XRD technique.

^d Calculated according to the $\alpha\text{-MnS}$ molar percentages derived from the K value method.

$\text{Mn}_x\text{Cd}_{1-x}\text{S}$ -based products with x higher than 0.20 are mainly composed by $\text{Mn}_{0.2}\text{Cd}_{0.8}\text{S}$ and $\alpha\text{-MnS}$, in which the molar percentage of $\alpha\text{-MnS}$ is increased upon enhancing the x values. For instance, the $\text{Mn}_x\text{Cd}_{1-x}\text{S}$ -based product with $x = 0.50$ is a heterojunction containing 38 mol% $\alpha\text{-MnS}$ and 62 mol% $\text{Mn}_{0.2}\text{Cd}_{0.8}\text{S}$ solid solution, while the $\text{Mn}_x\text{Cd}_{1-x}\text{S}$ -based product with $x = 0.75$ is a heterojunction containing 69 mol% $\alpha\text{-MnS}$ and 31 mol% $\text{Mn}_{0.2}\text{Cd}_{0.8}\text{S}$ solid solution. Moreover, the relative intensity of (002) diffraction peak is more strong and sharp than that of (100) and (110) peaks, which is different from the standard diffraction pattern of the hexagonal CdS as shown in Fig. 1a. It implies that CdS and $\text{Mn}_x\text{Cd}_{1-x}\text{S}$ preferably grow along [002] direction, which is possibly beneficial for the formation of nanorod-like shapes as mentioned below [20].

Fig. 2a shows the XRD patterns of the $\text{Mn}_x\text{Cd}_{1-x}\text{S}$ -based product with $x = 0.5$ ($\text{Mn}_{0.2}\text{Cd}_{0.8}\text{S}/\text{MnS}$ heterojunction with 38 mol% $\alpha\text{-MnS}$) modified with different MoS_2 contents. The single MoS_2 displays very weak diffraction peaks at $2\theta = 14.3^\circ$, 33.6° and 59.8° , which can be assigned to the reflections of (002), (100) and (110) planes of hexagonal MoS_2 (JCPDS No. 75-1539) [45], respectively. Nevertheless, no diffraction peaks of MoS_2 can be clearly identified from the XRD patterns of those MoS_2 -modified $\text{Mn}_{0.2}\text{Cd}_{0.8}\text{S}/\text{MnS}$ heterojunctions (denoted as $\text{MoS}_2\text{-Mn}_{0.2}\text{Cd}_{0.8}\text{S}/\text{MnS}$) even though the MoS_2 -loading content is enhanced to 20 wt%. Moreover, no obvious shift in those diffraction peaks of $\text{MoS}_2\text{-Mn}_{0.2}\text{Cd}_{0.8}\text{S}/\text{MnS}$ can be observed when enhancing the MoS_2 -loading contents from 1.0 wt% to 20 wt% (Fig. 2b). These results suggest that the one-pot solvothermal deposition process of MoS_2 does not influence the crystalline structure and composition of $\text{Mn}_{0.2}\text{Cd}_{0.8}\text{S}/\text{MnS}$ heterojunction, and the MoS_2 might exist as highly dispersed ultrathin nanosheets [44], which needs to be further validated by other

techniques.

3.2. Microstructure analyses

Fig. 3 shows the size and morphology of those $\text{Mn}_x\text{Cd}_{1-x}\text{S}$ -based products ($0 \leq x \leq 1.0$). As shown in Fig. 3a, the single CdS exhibits short nanorod-like morphology with a width of ~ 20 nm and a non-uniform length distribution. The presence of ethylenediamine with much lower dielectric constant (13.82) than that (78.2) of water during the present solvothermal process is in favor of one-dimensional CdS growth to the formation of CdS nanorods [47,48]. Nevertheless, the single $\alpha\text{-MnS}$ exhibits aggregated microsphere-like structures consisting of small sized nanoparticles (Fig. 3b). The $\text{Mn}_x\text{Cd}_{1-x}\text{S}$ -based product with $x = 0.25$ (Fig. 3c) has a similar nanorod-like morphology with slightly shorter length and co-existed some nanoparticles, and this changing trend in morphology is more obvious when further enhancing the x values to 0.50 and 0.75. Especially, the $\text{Mn}_x\text{Cd}_{1-x}\text{S}$ -based product with $x = 0.50$ is still mainly composed by nanorod-like structures with some nanoparticles located on the surface (Fig. 3d).

Since CdS displays nanorod-like morphology while $\alpha\text{-MnS}$ exhibits nanoparticle-like one during the present solvothermal process as mentioned above, it can be conjectured that $\text{Mn}_x\text{Cd}_{1-x}\text{S}$ -based product with $x = 0.50$ could form heterojunction structure, where those nanorod-like structures can be assigned to $\text{Mn}_{0.2}\text{Cd}_{0.8}\text{S}$, and those nanoparticles attached on nanorods would be $\alpha\text{-MnS}$, which can be validated by the following HRTEM observations. The $\text{Mn}_x\text{Cd}_{1-x}\text{S}$ -based product with $x = 0.75$ mainly contains nanoparticles co-existed with a small quantity of nanorods (Fig. 3e), which is consistent with the above results that this product is $\text{Mn}_{0.2}\text{Cd}_{0.8}\text{S}/\text{MnS}$ heterojunction, in which nanoparticle-

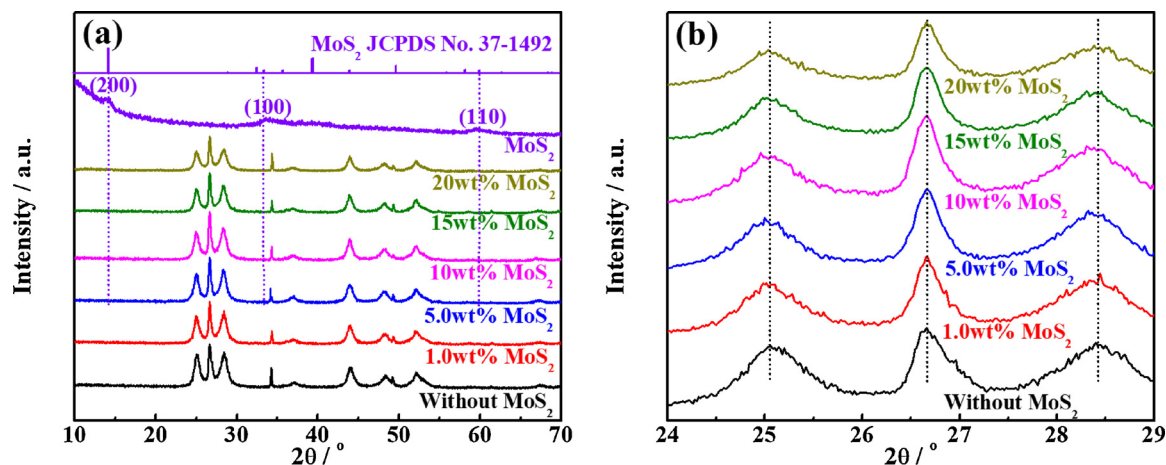


Fig. 2. (a) XRD patterns of the $\text{Mn}_{0.2}\text{Cd}_{0.8}\text{S}/\text{MnS}$ heterojunction modified with different MoS_2 contents. (b) XRD patterns at the lower angle region ($24^\circ < 2\theta < 29^\circ$) of figure (a).

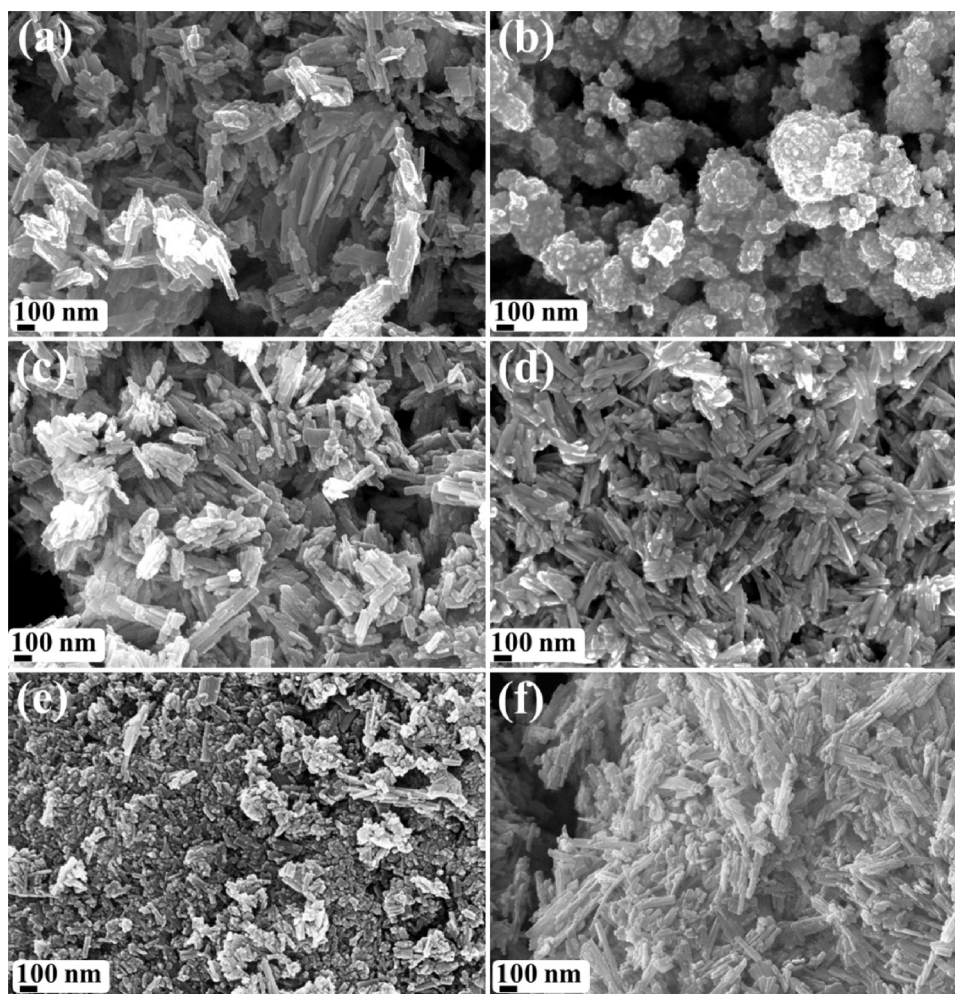


Fig. 3. FESEM images of the as-prepared CdS (a), MnS (b) and $\text{Mn}_x\text{Cd}_{1-x}\text{S}$ -based composites with $x = 0.25$ (c), 0.5 (d), 0.75 (e), and $15 \text{ wt}\%$ $\text{MoS}_2\text{-Mn}_{0.2}\text{Cd}_{0.8}\text{S/MnS}$ heterojunction (f).

like $\alpha\text{-MnS}$ has 69 mol% percentage (Table 1). After loading 15 wt% MoS_2 , no obvious difference could be identified between the shapes and nanostructures of $\text{Mn}_{0.2}\text{Cd}_{0.8}\text{S/MnS}$ heterojunction (Fig. 3f), suggesting that the MoS_2 loading dose not damage the heterojunction structure. The nanorod-like structures in those $\text{Mn}_x\text{Cd}_{1-x}\text{S}$ -based products with x value higher than 0.20 are consistent with the above XRD analysis results that the $\text{Mn}_{0.2}\text{Cd}_{0.8}\text{S}$ solid solution preferably grows along the [002] direction [49].

The heterostructures of 15 wt% $\text{MoS}_2\text{-Mn}_{0.2}\text{Cd}_{0.8}\text{S/MnS}$ with 38 mol% $\alpha\text{-MnS}$ can be further elucidated using TEM and HRTEM observations. As can be seen from Fig. 4a, the product is mainly composed by nanorods with lengths varying from 200 to 500 nm. From the HRTEM image (Fig. 4b), it can be found that the d -spacing (ca. 0.324 nm) of the nanorod's lattice fringes (as shown in the yellow square in Fig. 4b) is slightly lower than the d -spacing (0.336 nm) of (002) plane of hexagonal CdS, and thus it could be assigned to the (002) plane of $\text{Mn}_{0.2}\text{Cd}_{0.8}\text{S}$. Moreover, the Fast Fourier Transform (FFT) pattern (inset in the right upper corner of Fig. 4b) demonstrates that the nanorod has hexagonal crystal phase similar to CdS. It implies that Mn^{2+} ions with smaller radii might dope in the lattice, and thus lead to the decreases in d -spacing of CdS. In Fig. 4c, those nanoparticles attached on nanorod surface have lattice fringes with a d -spacing of ca. 0.261 nm (as shown in the red square in Fig. 4c), which can be ascribable to the (200) plane of $\alpha\text{-MnS}$. Also, the FFT pattern (inset in the right upper corner of Fig. 4c) indicates those nanoparticles with finite sizes are $\alpha\text{-MnS}$, which have excellent contacts with $\text{Mn}_{0.2}\text{Cd}_{0.8}\text{S}$ nanorod. Moreover, the (002)

planes of MoS_2 with a d -spacing of ca. 0.612 nm can also be observed from 15 wt% $\text{MoS}_2\text{-Mn}_{0.2}\text{Cd}_{0.8}\text{S/MnS}$ [50], suggesting the MoS_2 ultra-thin layers are intimately deposited on $\text{Mn}_{0.2}\text{Cd}_{0.8}\text{S}$ nanorod surface, as marked by blue circles in Fig. 4d. The TEM image (Fig. S1a) of 15 wt% $\text{MoS}_2\text{-Mn}_{0.2}\text{Cd}_{0.8}\text{S/MnS}$ with 38 mol% $\alpha\text{-MnS}$ shows the coexistence and intimate contacts of nanorod bundle, nanoparticles and ultrathin nanoflakes, and its energy dispersive X-ray (EDX) element mappings (Fig. 4e–h) illustrate that the uniform distribution of Cd, Mn, S and Mo atoms, which is consistent to the above analysis results. The excellent interfaces among $\alpha\text{-MnS}$ nanoparticle, $\text{Mn}_{0.2}\text{Cd}_{0.8}\text{S}$ nanorod and MoS_2 thin layers are expected to not only improve the charge separation but also provide abundant catalytic sites for H_2 production reactions.

From the liquid N_2 adsorption-desorption isotherms (Fig. S2), it can be seen that both 15 wt% $\text{MoS}_2\text{-Mn}_{0.2}\text{Cd}_{0.8}\text{S/MnS}$ and $\text{Mn}_{0.2}\text{Cd}_{0.8}\text{S/MnS}$ heterojunctions with 38 mol% $\alpha\text{-MnS}$ have type IV isotherms, and their type H_2 hysteresis loops indicate the existences of mesopores and micropores. In addition, $\text{MoS}_2\text{-Mn}_{0.2}\text{Cd}_{0.8}\text{S/MnS}$ heterojunction has a specific surface area of $48.3 \text{ m}^2 \text{ g}^{-1}$, larger than that ($38.0 \text{ m}^2 \text{ g}^{-1}$) of the pristine $\text{Mn}_{0.2}\text{Cd}_{0.8}\text{S/MnS}$. Also, $\text{MoS}_2\text{-Mn}_{0.2}\text{Cd}_{0.8}\text{S/MnS}$ heterojunction exhibits a broader pore size distribution centered at $\sim 43 \text{ nm}$ as compared to $\text{Mn}_{0.2}\text{Cd}_{0.8}\text{S/MnS}$ (inset in Fig. S2). Namely, the modification of MoS_2 through the one-step solvothermal process can increase both of the specific surface area and the pore size of $\text{Mn}_{0.2}\text{Cd}_{0.8}\text{S/MnS}$ heterojunction, which would be a benefit to the improvement of photocatalytic performance.

The survey X-ray photoelectron spectrum (XPS, Fig. S3) of 15 wt%

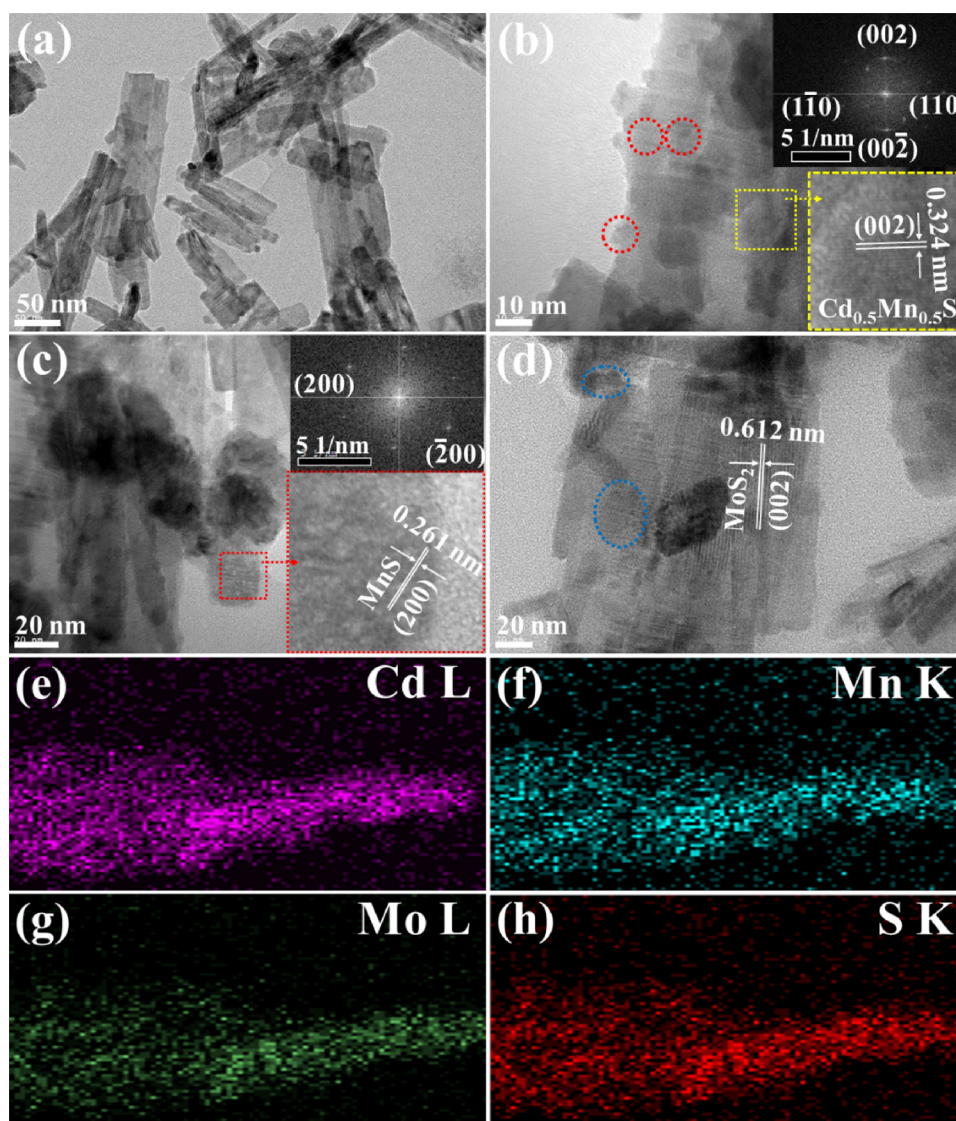


Fig. 4. TEM and HRTEM images (a–d) of the 15 wt% $\text{MoS}_2\text{-Mn}_{0.2}\text{Cd}_{0.8}\text{S/MnS}$ heterojunction with 38 mol% $\alpha\text{-MnS}$ and the corresponding EDX element mappings of Cd (e), Mn (f), Mo (g), and S (h). (For interpretation of the references to colour in the text, the reader is referred to the web version of this article.)

$\text{MoS}_2\text{-Mn}_{0.2}\text{Cd}_{0.8}\text{S/MnS}$ heterojunction with 38 mol% $\alpha\text{-MnS}$ displays the presence of Mn, Cd, Mo and S [27,34]. For comparison, the survey XPS spectra of the pristine $\text{Mn}_{0.2}\text{Cd}_{0.8}\text{S/MnS}$, the single MoS_2 and $\alpha\text{-MnS}$ are also depicted in Fig. S3. As can be seen, the pristine $\text{Mn}_{0.2}\text{Cd}_{0.8}\text{S/MnS}$ and the single $\alpha\text{-MnS}$ show no any binding energy peak of Mo 3d, indicating no MoS_2 existing in those samples. The valence states of Mn, Cd, Mo and S in those samples can be determined from the high-resolution XPS spectra (Fig. 5). Cd3d XPS spectra (Fig. 5a) of both 15 wt% $\text{MoS}_2\text{-Mn}_{0.2}\text{Cd}_{0.8}\text{S/MnS}$ and $\text{Mn}_{0.2}\text{Cd}_{0.8}\text{S/MnS}$ heterojunctions present two symmetrical peaks with binding energies at 404.5 and 411.2 eV, corresponding to $\text{Cd}3d_{5/2}$ and $\text{Cd}3d_{3/2}$ [34], respectively. It indicates the +2 oxidation state of Cd in those $\text{Mn}_{0.2}\text{Cd}_{0.8}\text{S/MnS}$ heterojunctions. Mn2p XPS spectra (Fig. 5b) of both 15 wt% $\text{MoS}_2\text{-Mn}_{0.2}\text{Cd}_{0.8}\text{S/MnS}$ and $\text{Mn}_{0.2}\text{Cd}_{0.8}\text{S/MnS}$ heterojunctions give two characteristic peaks with binding energies at 640.6 ($\text{Mn}2p_{3/2}$) and 651.8 ($\text{Mn}2p_{1/2}$) eV in addition to a shoulder at 642.2 eV, which can be assigned to Mn^{2+} in the composite [34,51]. Compared to the single $\alpha\text{-MnS}$ with Mn2p signal at 640.8 and 652.2 eV, the shifts toward lower energy of both 15 wt% $\text{MoS}_2\text{-Mn}_{0.2}\text{Cd}_{0.8}\text{S/MnS}$ and $\text{Mn}_{0.2}\text{Cd}_{0.8}\text{S/MnS}$ heterojunctions indicate the possible interaction between $\alpha\text{-MnS}$ nanoparticles and $\text{Mn}_{0.2}\text{Cd}_{0.8}\text{S}$ nanorods as well as the different chemical species of Mn^{2+} ions. In addition, S2p spectra (Fig. 5c) of both

15 wt% $\text{MoS}_2\text{-Mn}_{0.2}\text{Cd}_{0.8}\text{S/MnS}$ and $\text{Mn}_{0.2}\text{Cd}_{0.8}\text{S/MnS}$ heterojunctions can be deconvoluted into two apparent symmetrical peaks with binding energies at 160.9 ($\text{S}2p_{3/2}$) and 162.1 eV ($\text{S}2p_{1/2}$), indicating that the S exists as -2 oxidation state [34,52]. Those binding energies of S2p are lower than that of MoS_2 (161.0 and 162.2 eV) and $\alpha\text{-MnS}$ (161.1 and 162.3 eV), which further confirmed the strong interactions among $\alpha\text{-MnS}$, MoS_2 and $\text{Mn}_{0.2}\text{Cd}_{0.8}\text{S}$. Moreover, Mo3d spectra (Fig. 5d) of both 15 wt% $\text{MoS}_2\text{-Mn}_{0.2}\text{Cd}_{0.8}\text{S/MnS}$ and $\text{Mn}_{0.2}\text{Cd}_{0.8}\text{S/MnS}$ heterojunctions can be divided into two peaks, the binding energy peaks at 228.1 and 231.2 eV corresponds to $\text{Mo}^{4+}3d_{5/2}$ and $\text{Mo}^{4+}3d_{3/2}$ [53], which are similar to that of the single MoS_2 . It indicates that Mo^{4+} is the dominant oxidation state and MoS_2 is deposited on the $\text{Mn}_{0.2}\text{Cd}_{0.8}\text{S/MnS}$ heterostructure. The above binding energies of Cd, Mn, Mo and S are in good agreement with the reported values [30,31,34,35,53].

3.3. Absorption spectra analyses

Fig. 6 presents the UV–vis diffuse reflectance absorption spectra (DRS) of the as-prepared CdS, $\alpha\text{-MnS}$ and $\text{Mn}_{0.2}\text{Cd}_{0.8}\text{S/MnS}$ heterojunctions modified with different MoS_2 contents. The single CdS has an onset of absorption edge at around 536 nm (Fig. 6a), corresponding to a bandgap energy of ~ 2.32 eV, which is comparable to the reported

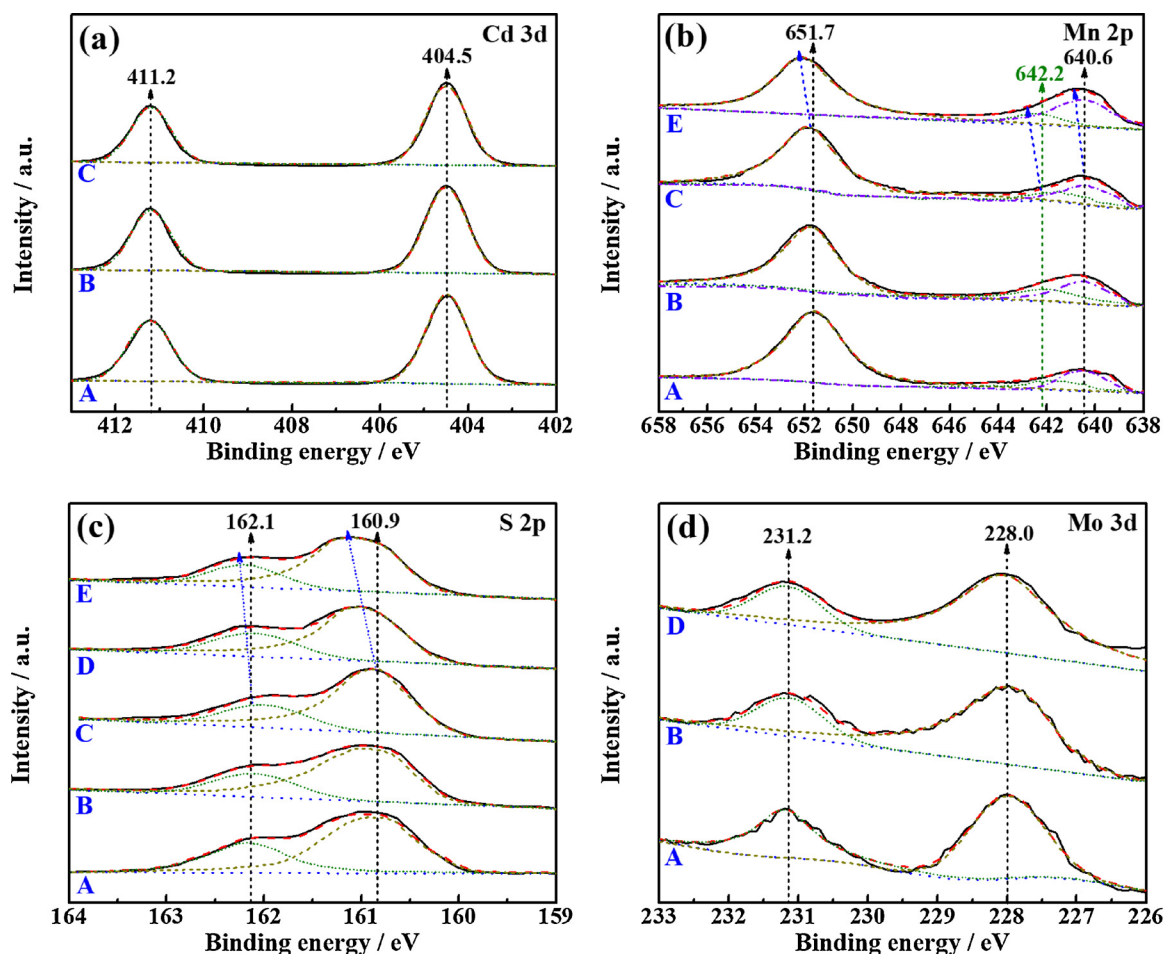


Fig. 5. Comparisons of Cd 3d (a), Mn 2p (b), S 2p (c), and Mo 3d (d) XPS spectra of 15 wt% $\text{MoS}_2\text{-Mn}_{0.2}\text{Cd}_{0.8}\text{S}/\text{MnS}$ heterojunction with 38 mol% $\alpha\text{-MnS}$ before (A) and after (B) 20 h irradiation for the photoreaction, the pristine $\text{Mn}_{0.2}\text{Cd}_{0.8}\text{S}/\text{MnS}$ (C), the single MoS_2 (D) and $\alpha\text{-MnS}$ (E).

value for the standard bulk CdS sample (~ 2.40 eV) [14]. The absorption edge of $\alpha\text{-MnS}$ locates at around 480 nm, corresponding to a band gap of ~ 2.58 eV (Fig. 6a), which is similar to the reported one (~ 2.57 eV) [51]. The three additional absorption peaks centered at ca. 450, 517 and 611 nm for $\alpha\text{-MnS}$ can be due to the internal transitions in the partly occupied 3d states of Mn and the bulk defects in crystals [27,51]. Along with enhancing the x value, those $\text{Mn}_x\text{Cd}_{1-x}\text{S}$ -based products show an increasing absorption in the visible region, and the

band gap energies of each sample were calculated from the onsets of absorption edges as shown in Table S1. From CdS to $\text{Mn}_x\text{Cd}_{1-x}\text{S}$ -based product with $x = 0.75$, the band gap energy only changes ~ 0.16 eV, which is consistent with the slight shift of diffraction peaks to higher angles as shown in Fig. 1a. It provides another piece of evidence that very limited $\alpha\text{-MnS}$ amounts dissolve in the CdS lattice during the present solvothermal process [27], and the additional Mn^{2+} ions can form thermodynamically stable $\alpha\text{-MnS}$ in addition to the $\text{Mn}_{0.2}\text{Cd}_{0.8}\text{S}$

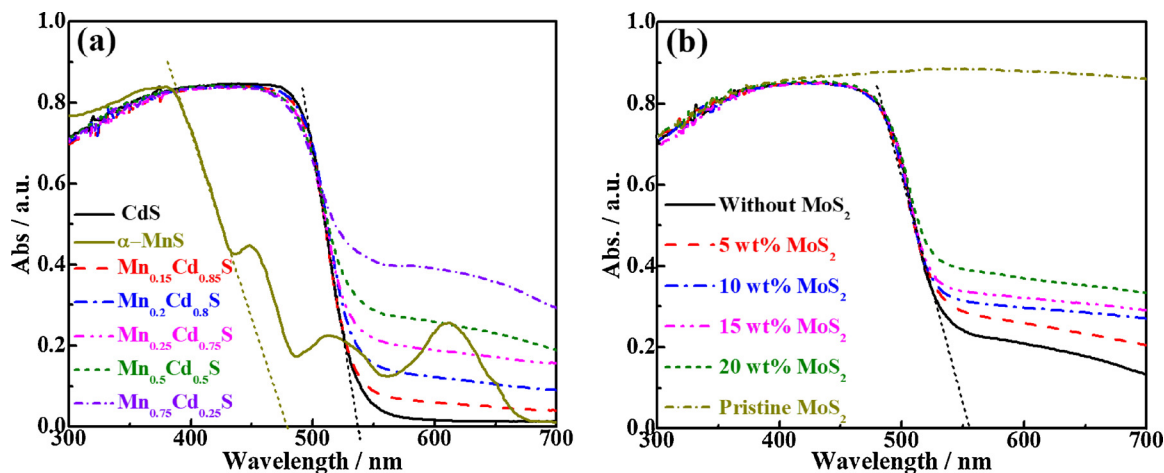


Fig. 6. (a) DRS spectra of the as-prepared CdS, $\alpha\text{-MnS}$ and $\text{Mn}_x\text{Cd}_{1-x}\text{S}$ -based products with different x values. (b) DRS spectra of the $\text{Mn}_{0.2}\text{Cd}_{0.8}\text{S}/\text{MnS}$ heterojunction modified with different MoS_2 contents.

solid solution as mentioned above. Along with enhancing the x value (Mn percentage), a more flat absorption can be observed at $\lambda > 500$ nm, implying that the formed α -MnS in those $\text{Mn}_x\text{Cd}_{1-x}\text{S}$ -based products would contribute the light absorption due to the formation of heterojunctions between α -MnS and $\text{Mn}_{0.2}\text{Cd}_{0.8}\text{S}$ solid solution.

As mentioned above, the $\text{Mn}_x\text{Cd}_{1-x}\text{S}$ -based product with $x = 0.50$ is a $\text{Mn}_{0.2}\text{Cd}_{0.8}\text{S}/\text{MnS}$ heterojunction containing 38 mol% α -MnS, which displays an absorption edge around 555 nm, corresponding to the band gap of ~ 2.23 eV (Table S1). After modified with MoS_2 via the one-pot solvothermal process, the $\text{MoS}_2\text{-Mn}_{0.2}\text{Cd}_{0.8}\text{S}/\text{MnS}$ composites show enhanced background absorptions in the range of 500–800 nm (Fig. 6b), which exhibit an increasing trend along with enhancing the MoS_2 content. The elevated backgrounds might be due to the enhancement of the deposited MoS_2 content since the as-synthesized MoS_2 has intensive absorptions in the visible region due to its narrow band gap [34]. Therefore, the light harvesting efficiency of $\text{MoS}_2\text{-Mn}_{0.2}\text{Cd}_{0.8}\text{S}/\text{MnS}$ composites are higher than that of the pristine $\text{Mn}_{0.2}\text{Cd}_{0.8}\text{S}/\text{MnS}$ in the visible region. It is believed that the enhanced light absorption of $\text{MoS}_2\text{-Mn}_{0.2}\text{Cd}_{0.8}\text{S}/\text{MnS}$ is favorable to generate more available photogenerated electrons for participating in the photocatalytic H_2 evolution reactions [34], which will be further discussed below.

3.4. Photocatalytic performance analyses

Using $\text{Mn}_{0.2}\text{Cd}_{0.8}\text{S}/\text{MnS}$ heterojunction containing 38 mol% α -MnS as a reference, the photoreaction conditions for H_2 production were optimized under visible light ($\lambda \geq 420$ nm) irradiation in the presence of Na_2S (0.35 M) and Na_2SO_3 (0.25 M) mixed solution. Under the optimized photoreaction condition, the pure α -MnS only shows very limited H_2 production activity under $\lambda \geq 420$ nm light irradiation as shown in Fig. 7a. With enhancing the x value from 0 to 0.50, the $\text{Mn}_x\text{Cd}_{1-x}\text{S}$ -based products show an increasing H_2 production activity, which then slightly decreases once the x value is enhanced to 0.75 and 1.0. This changing trend of activity for $\text{Mn}_x\text{Cd}_{1-x}\text{S}$ -based products along with enhancing the x values can be ascribed to the changes in composition and morphology, which could influence the surface feature, optical absorption and charge generation/separation processes. For instance, the activity of $\text{Mn}_x\text{Cd}_{1-x}\text{S}$ -based products shows a slightly increasing trend along with enhancing the x value from 0 (the single CdS) to 0.20 due to the formation of $\text{Mn}_x\text{Cd}_{1-x}\text{S}$ solid solution [29–34]. Once the x value is enhanced to 0.25, the corresponding $\text{Mn}_x\text{Cd}_{1-x}\text{S}$ -based product transforms into $\text{Mn}_{0.2}\text{Cd}_{0.8}\text{S}/\text{MnS}$ heterojunction containing 5.7 mol% α -MnS (Table 1), which might be a benefit to the

photogenerated charge separation, and thus causing more significantly enhanced H_2 production activity as shown in Fig. 7a. Upon enhancing α -MnS to 38 mol%, the corresponding $\text{Mn}_{0.2}\text{Cd}_{0.8}\text{S}/\text{MnS}$ heterojunction ($\text{Mn}_x\text{Cd}_{1-x}\text{S}$ -based product with $x = 0.50$, Table 1) exhibits the best H_2 production activity of $335 \mu\text{mol h}^{-1}$, which is 1.95 times higher than that ($171 \mu\text{mol h}^{-1}$) of the single CdS under $\lambda \geq 420$ nm light irradiation. The decreased activity of $\text{Mn}_x\text{Cd}_{1-x}\text{S}$ -based product with $x = 0.75$ can be due to the excessively coexisted α -MnS (up to 69 mol%, Table 1), which has very lower H_2 production activity compared to the pure CdS as shown in Fig. 7a.

Fig. 7b depicts the effect of MoS_2 modification on the photoactivity of $\text{Mn}_{0.2}\text{Cd}_{0.8}\text{S}/\text{MnS}$ heterojunction with 38 mol% α -MnS. After modifying with only 1.0 wt% MoS_2 on $\text{Mn}_{0.2}\text{Cd}_{0.8}\text{S}/\text{MnS}$, the H_2 production activity is significantly enhanced from 335 to $513 \mu\text{mol h}^{-1}$, which can be further improved along with the increase of MoS_2 loading content. Especially, 15 wt% $\text{MoS}_2\text{-Mn}_{0.2}\text{Cd}_{0.8}\text{S}/\text{MnS}$ composite shows the highest H_2 production activity of $995 \mu\text{mol h}^{-1}$, which is about 2.97 times higher than that of the pristine $\text{Mn}_{0.2}\text{Cd}_{0.8}\text{S}/\text{MnS}$ heterojunction. Further enhancing the MoS_2 loading content to 20 wt%, the $\text{MoS}_2\text{-Mn}_{0.2}\text{Cd}_{0.8}\text{S}/\text{MnS}$ exhibits a decreased activity, possibly attributable to the excessively loaded MoS_2 cocatalyst, which would shield the incident light from illuminating the photocatalyst and hinder the effective contact between the active sites and the reactants [34]. These results demonstrate that an appropriate MoS_2 loading content can optimize the activity of $\text{Mn}_{0.2}\text{Cd}_{0.8}\text{S}/\text{MnS}$ heterojunction. For comparison, the commonly used noble metal Pt cocatalysts was also loaded on $\text{Mn}_{0.2}\text{Cd}_{0.8}\text{S}/\text{MnS}$ heterojunction with 38 mol% α -MnS via the conventional photo-deposition method [8,9], and the Pt nanoparticles with average size of ~ 10 nm are uniformly dispersed on those $\text{Mn}_{0.2}\text{Cd}_{0.8}\text{S}$ nanorod surfaces (Fig. S4). As shown in Fig. 7b, 1.0 wt% Pt- $\text{Mn}_{0.2}\text{Cd}_{0.8}\text{S}/\text{MnS}$ shows a H_2 production activity of $868 \mu\text{mol h}^{-1}$, which is much higher than that of $\text{Mn}_{0.2}\text{Cd}_{0.8}\text{S}/\text{MnS}$ heterojunction alone, but is still lower than that ($995 \mu\text{mol h}^{-1}$) of 15 wt% $\text{MoS}_2\text{-Mn}_{0.2}\text{Cd}_{0.8}\text{S}/\text{MnS}$. It demonstrates that MoS_2 is a promising highly efficient cocatalyst for improving the photocatalytic H_2 evolution in the present system.

3.5. Photostability analyses of 15 wt% $\text{MoS}_2\text{-Mn}_{0.2}\text{Cd}_{0.8}\text{S}/\text{MnS}$ heterojunction

To confirm the recycling stability for H_2 production over 15 wt% $\text{MoS}_2\text{-Mn}_{0.2}\text{Cd}_{0.8}\text{S}/\text{MnS}$, five consecutive H_2 production runs for total 20 h irradiation was performed under the same conditions. Each cycle was performed for 4 h under $\lambda \geq 420$ nm light irradiation. As can be seen from Fig. 8a, 15 wt% $\text{MoS}_2\text{-Mn}_{0.2}\text{Cd}_{0.8}\text{S}/\text{MnS}$ achieves an average H_2 production activity of $951 \mu\text{mol h}^{-1}$ in the first run of 4 h

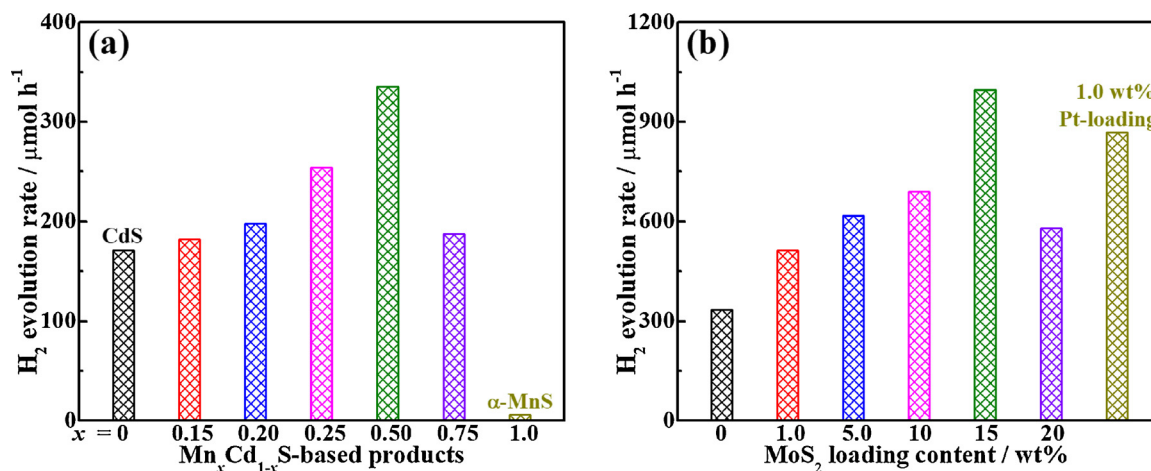


Fig. 7. (a) H_2 production activity of CdS, α -MnS and $\text{Mn}_x\text{Cd}_{1-x}\text{S}$ -based products with different x values. (b) H_2 production activity of $\text{Mn}_{0.2}\text{Cd}_{0.8}\text{S}/\text{MnS}$ heterojunction modified with different MoS_2 contents. Conditions: catalyst (0.05 g) in Na_2S (0.35 M) and Na_2SO_3 (0.25 M) mixed solution (50 mL), $\lambda \geq 420$ nm light irradiation.

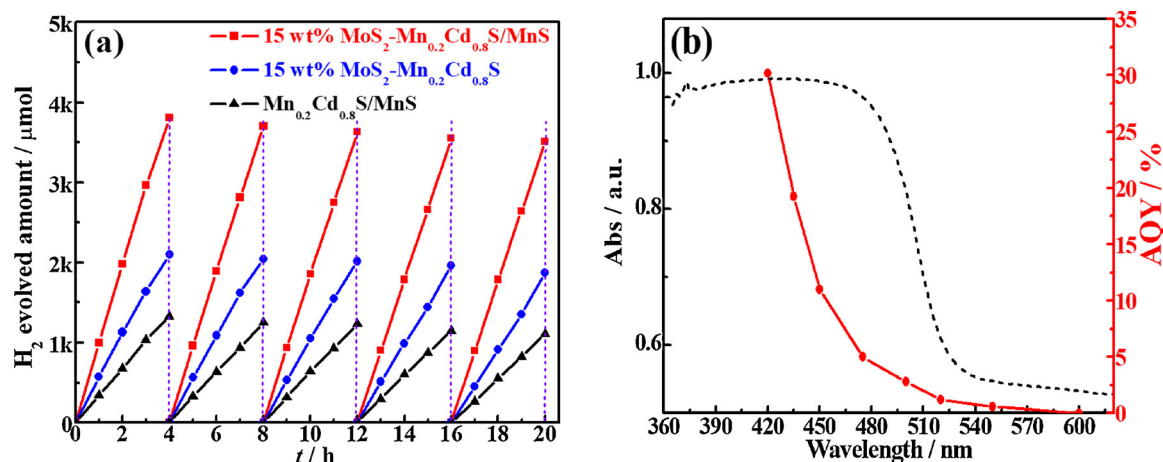


Fig. 8. (a) Time course of the H₂ production over 15 wt% MoS₂-Mn_{0.2}Cd_{0.8}S/MnS, 15 wt% MoS₂-Mn_{0.2}Cd_{0.8}S and Mn_{0.2}Cd_{0.8}S/MnS. (b) AQY values and DRS spectrum of 15 wt% MoS₂-Mn_{0.2}Cd_{0.8}S/MnS. Conditions: catalyst (0.05 g) in Na₂S (0.35 M) and Na₂SO₃ (0.25 M) mixed solution (50 mL), λ ≥ 420 nm light irradiation.

photoreaction, which then slightly decreases to 926, 908, 887 and 876 μmol h⁻¹ in the second, third, fourth and fifth run, respectively. The percentages of the average activity of the second, third, fourth and fifth run as compared with the first run can be calculated to be 97.4%, 95.5%, 93.3% and 92.1%, respectively. Comparatively, single Mn_{0.2}Cd_{0.8}S/MnS shows a lower average H₂ production activity of 332 μmol h⁻¹ in the first run of 4 h photoreaction, and the percentages of the average activity of the second, third, fourth and fifth run as compared with the first run can be estimated to be 94.3%, 93.1%, 86.1% and 83.4%, respectively.

To further check the photostability of 15 wt% MoS₂-Mn_{0.2}Cd_{0.8}S/MnS heterojunction, the photocatalyst after the 20 h photoreaction for H₂ production was recovered. As observed from Fig. S5a, the XRD pattern of the recovered product is essentially similar to that of the original one, and no obvious shift in those diffraction peak locations. Also, the low-magnification TEM image (Fig. S5b) shows that the recovered 15 wt% MoS₂-Mn_{0.2}Cd_{0.8}S/MnS after the 20 h photoreaction still maintains the nanorod morphology coexisting with some nanoparticles, which is similar to the original one as shown in Fig. 4a. Moreover, both of the survey XPS spectra (Fig. S3) for 15 wt% MoS₂-Mn_{0.2}Cd_{0.8}S/MnS before and after the 20 h photoreaction only display the presence of Mn, Cd, Mo and S with no evident peak of other elements (for example, O1s at 531.8 eV) [27,34], and those high-resolution Cd3d, Mn2p, S2p and Mo3d spectra (Fig. 5) of the recovered 15 wt % MoS₂-Mn_{0.2}Cd_{0.8}S/MnS are also very similar to that of the original one, indicating that the element composition and valence states of MoS₂-Mn_{0.2}Cd_{0.8}S/MnS are unchanged during the long-term photoreaction process.

The above results indicate that MoS₂ modification not only boosts the photoactivity of Mn_{0.2}Cd_{0.8}S/MnS heterojunction, but also improve the photostability in the present photoreaction system. Moreover, 15 wt % MoS₂-Mn_{0.2}Cd_{0.8}S achieves an average H₂ production activity of 525 μmol h⁻¹ in the first run of 4 h photoreaction with 89.3% average activity remained after the fifth run. Although this activity is much higher than that (198 μmol h⁻¹, please ref. Fig. 7a) of the single Mn_{0.2}Cd_{0.8}S (Mn_xCd_{1-x}S-based products with x = 0.20, in which there is no α-MnS as mentioned above) due to the MoS₂ modification, it is still much lower than that of the 15 wt% MoS₂-Mn_{0.2}Cd_{0.8}S/MnS (Fig. 8a), implying that the formation of heterojunction between Mn_{0.2}Cd_{0.8}S solid solution and α-MnS can improve both the photocatalytic activity and stability for H₂ production. Also, the wavelength-dependent AQY values match with the absorption edge of 15 wt% MoS₂-Mn_{0.2}Cd_{0.8}S/MnS (Fig. 8b), and the AQY values is up to 30.2% at 420 nm light irradiation, much higher than that (ca. 25–23.7%) of the reported Mn_xCd_{1-x}S at 420 nm light irradiation [30–34]. Also, the

present AQY value of 30.2% at 420 nm light irradiation is a relatively high one among those sulfide-based photocatalysts reported in the last three years (Table S2).

3.6. Energy band structure and photocatalytic mechanism analyses

To investigate the energy band structures of α-MnS and Mn_{0.2}Cd_{0.8}S solid solution in the Mn_xCd_{1-x}S-based product with x = 0.50, the flat-band potentials (*E*_{fb}) values of the single α-MnS and Mn_{0.2}Cd_{0.8}S solid solution were determined using the Mott – Schottky relation [12]:

$$C^{-2} = (2/e\epsilon\epsilon_0 N_d) [V_a - E_{fb} - kT/e]$$

where, *C* is space charge layer capacitance, *e* is electron charge, *ε* is dielectric constant, *ε*₀ is permittivity of vacuum, *N*_d is electron donor density, *V*_a is the applied potential, and *E*_{fb} is flat band potential.

As can be seen for Fig. S6, all Mott – Schottky plots of the α-MnS film have the same intercept with the X-axis, indicating that the *E*_{fb} value is -1.39 V vs. Ag/AgCl (saturated KCl solution, *E*⁰ = 0.198 V vs. NHE) [54,55], and thus its *E*_{fb} value can be calculated to be -1.39 + 0.198 = -1.19 V vs. NHE. Since the conduction band (CB) bottom is more negative by ca. -0.1 V than *E*_{fb} for certain n-type semiconductors [56], the CB level (*E*_{CB}) of α-MnS can be estimated to be ca. -1.29 V [12,55]. As mentioned above, the absorption edge of α-MnS locates at around 480 nm, corresponding to a band gap (*E*_g) of ~2.58 eV (Fig. 6a), and thus its valence band (VB) level (*E*_{VB}) can be calculated to be +1.29 V according to the formula (*E*_{VB} = *E*_g + *E*_{CB}) [54,55]. Similarly, the Mott – Schottky plots (Fig. S6) of the Mn_{0.2}Cd_{0.8}S solid solution film indicate that the *E*_{fb} value is -0.82 + 0.198 = -0.62 V vs. NHE, and thus its *E*_{CB} value can be estimated to be ca. -0.62 + (-0.1) = -0.72 V. Since Mn_{0.2}Cd_{0.8}S solid solution has a *E*_g value of ~2.27 eV (Table S1) calculated from the DRS spectrum shown in Fig. 6a, its *E*_{VB} value can be estimated to be ca. +1.55 V according to the formula (*E*_{VB} = *E*_g + *E*_{CB}) [54,55]. Therefore, the potential energy diagrams for α-MnS and Mn_{0.2}Cd_{0.8}S solid solution can be drawn as Fig. 9.

As can be seen, both α-MnS and Mn_{0.2}Cd_{0.8}S have *E*_{CB} levels negative than the reduction potential of H⁺/H₂, and the *E*_{CB} (-1.29 V) of the α-MnS is more negative than the *E*_{CB} level (-0.72 V) of the Mn_{0.2}Cd_{0.8}S, demonstrating the thermodynamic feasibility for the photogenerated electron transferring from α-MnS to Mn_{0.2}Cd_{0.8}S and then to MoS₂ for photocatalytic H₂ production reaction under visible light irradiation. Also, Mn_{0.2}Cd_{0.8}S provides a sufficiently positive *E*_{VB} level (+1.55 V) compared to the α-MnS's VB (+1.29 V) as mentioned above. It is a benefit to the photogenerated charge separation in space for promoting the H₂ production reactions, and thus a possible heterojunction-based

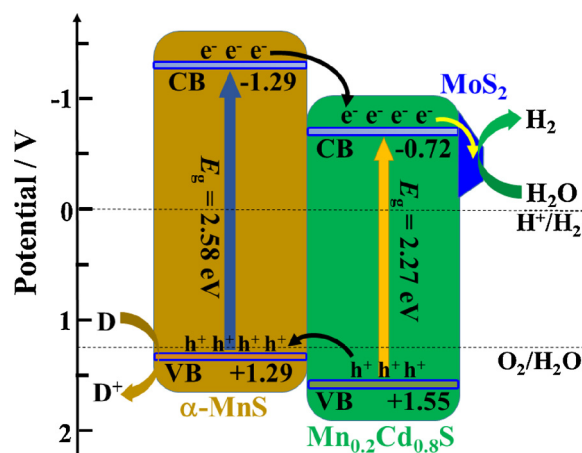


Fig. 9. Energy band diagrams of α -MnS and $\text{Mn}_{0.2}\text{Cd}_{0.8}\text{S}$ solid solution in $\text{Mn}_{0.2}\text{Cd}_{0.8}\text{S}/\text{MnS}$ heterojunction and its probable photocatalytic mechanism for H_2 production.

photocatalytic mechanism for H_2 production over the present $\text{MoS}_2\text{-Mn}_{0.2}\text{Cd}_{0.8}\text{S}/\text{MnS}$ composite is proposed in Fig. 9. Namely, the well aligned energy band structures (Fig. 9) and the intimate interfacial contacts among $\text{Mn}_{0.2}\text{Cd}_{0.8}\text{S}$, α -MnS and MoS_2 (Fig. 4) facilitate the photoinduced electron transferring from α -MnS to $\text{Mn}_{0.2}\text{Cd}_{0.8}\text{S}$ and then to MoS_2 , thus promoting the charge separation for H_2 production reaction.

The above conjecture can be validated by the photoluminescence (PL) spectra under excitation wavelength of 426 nm (Fig. 10a). 15 wt% $\text{MoS}_2\text{-Mn}_{0.2}\text{Cd}_{0.8}\text{S}/\text{MnS}$ has the lowest PL peak intensity compared to 15 wt% $\text{MoS}_2\text{-Mn}_{0.2}\text{Cd}_{0.8}\text{S}$ and $\text{Mn}_{0.2}\text{Cd}_{0.8}\text{S}$ alone. It indicates the formation of heterojunction between $\text{Mn}_{0.2}\text{Cd}_{0.8}\text{S}$ solid solution and α -MnS can promote the photogenerated charge transfer/separation at interface, and MoS_2 modification leads to faster photogenerated charge transfer/separation dynamics due to intimate contact of MoS_2 and $\text{Mn}_{0.2}\text{Cd}_{0.8}\text{S}$ (Fig. 4). This consequence can also be proved by Fig. 10b, in which the pristine 15 wt% $\text{MoS}_2\text{-Mn}_{0.2}\text{Cd}_{0.8}\text{S}/\text{MnS}$ without the photoreaction for H_2 production the exhibits the largest photocurrent response among those products under $\lambda \geq 420$ nm light irradiation, demonstrating that 15 wt% $\text{MoS}_2\text{-Mn}_{0.2}\text{Cd}_{0.8}\text{S}/\text{MnS}$ has more efficient charge transfer/separation processes. Electrochemical impedance spectra (EIS) of $\text{Mn}_{0.2}\text{Cd}_{0.8}\text{S}/\text{MnS}$ and its MoS_2 -modified product were used to further investigate the migration and interface transfer/recombination rates of charge carriers. It was found that the $\text{MoS}_2\text{-Mn}_{0.2}\text{Cd}_{0.8}\text{S}/\text{MnS}$ composite exhibits much smaller arc sizes in the

middle-frequency region as compared to the pristine $\text{Mn}_{0.2}\text{Cd}_{0.8}\text{S}/\text{MnS}$ under both dark and light irradiation (Fig. S7). It demonstrates that the $\text{MoS}_2\text{-Mn}_{0.2}\text{Cd}_{0.8}\text{S}/\text{MnS}$ has faster electron transfer through an intimate interface between $\text{Mn}_{0.2}\text{Cd}_{0.8}\text{S}/\text{MnS}$ and MoS_2 as compared to the pristine $\text{Mn}_{0.2}\text{Cd}_{0.8}\text{S}/\text{MnS}$, which is in good agreement with the photocatalytic performance.

According to the diagram of energy band structures shown in Fig. 9, both $\text{Mn}_{0.2}\text{Cd}_{0.8}\text{S}$ and α -MnS in $\text{MoS}_2\text{-Mn}_{0.2}\text{Cd}_{0.8}\text{S}/\text{MnS}$ heterojunction can be excited under $\lambda \geq 420$ nm light irradiation, and the photo-induced electrons can transfer from α -MnS to $\text{Mn}_{0.2}\text{Cd}_{0.8}\text{S}$, which causing the faster charge separation and the higher photocurrent response. Nevertheless, the single $\text{Mn}_{0.2}\text{Cd}_{0.8}\text{S}$ has no such directional electron transfer channel, and thus causing more severe charge recombination and the lower photocurrent response. Also, the cocatalyst MoS_2 loading on $\text{Mn}_{0.2}\text{Cd}_{0.8}\text{S}/\text{MnS}$ accelerates the photogenerated charge separation and provided abundant reactive sites [34], contributing to the outstanding H_2 production activity. Meantime, the holes in the VB of $\text{Mn}_{0.2}\text{Cd}_{0.8}\text{S}$ would be transferred to α -MnS and trapped by the sacrificial reagents, further boosting the charge separation. Overall, the well aligned energy band structures and the intimate interfacial contacts among $\text{Mn}_{0.2}\text{Cd}_{0.8}\text{S}$, α -MnS and MoS_2 facilitate the photoinduced electron transferring from the nanoparticle-like α -MnS to the nanorod-like $\text{Mn}_{0.2}\text{Cd}_{0.8}\text{S}$ and then to the nanoflake-like MoS_2 , thus promoting the charge separation and providing more active sites for H_2 production reaction.

4. Conclusions

In summary, a series of novel MoS_2 -modified $\text{Mn}_x\text{Cd}_{1-x}\text{S}$ -based products have been successfully fabricated via a facile one-pot solvothermal process. The material characterization results indicate that the $\text{Mn}_x\text{Cd}_{1-x}\text{S}$ -based products can transform into novel heterojunctions consisting of nanorod-like $\text{Mn}_{0.2}\text{Cd}_{0.8}\text{S}$ solid solution and nanoparticle-like α -MnS by enhancing the x value from 0.20 to 0.75, and the resulted $\text{Mn}_{0.2}\text{Cd}_{0.8}\text{S}/\text{MnS}$ heterojunction containing 38 mol% α -MnS demonstrates an optimum composition ratio with a much better H_2 production activity ($335 \mu\text{mol h}^{-1}$) than that ($171 \mu\text{mol h}^{-1}$) of the single CdS under visible light ($\lambda \geq 420$ nm) irradiation. The modification with MoS_2 via a one-pot solvothermal process can significantly improve the photocatalytic performance of the $\text{Mn}_{0.2}\text{Cd}_{0.8}\text{S}/\text{MnS}$ heterojunction, and 15 wt% $\text{MoS}_2\text{-Mn}_{0.2}\text{Cd}_{0.8}\text{S}/\text{MnS}$ composite achieves the best H_2 production activity of $995 \mu\text{mol h}^{-1}$, which is 2.97 times higher than that of the $\text{Mn}_{0.2}\text{Cd}_{0.8}\text{S}/\text{MnS}$ alone. Moreover, the MoS_2 modification results in an improved H_2 production performance that exceeds Pt metal loading. The well aligned energy band structures and the intimate interfacial contacts among $\text{Mn}_{0.2}\text{Cd}_{0.8}\text{S}$, α -MnS and MoS_2 facilitate the

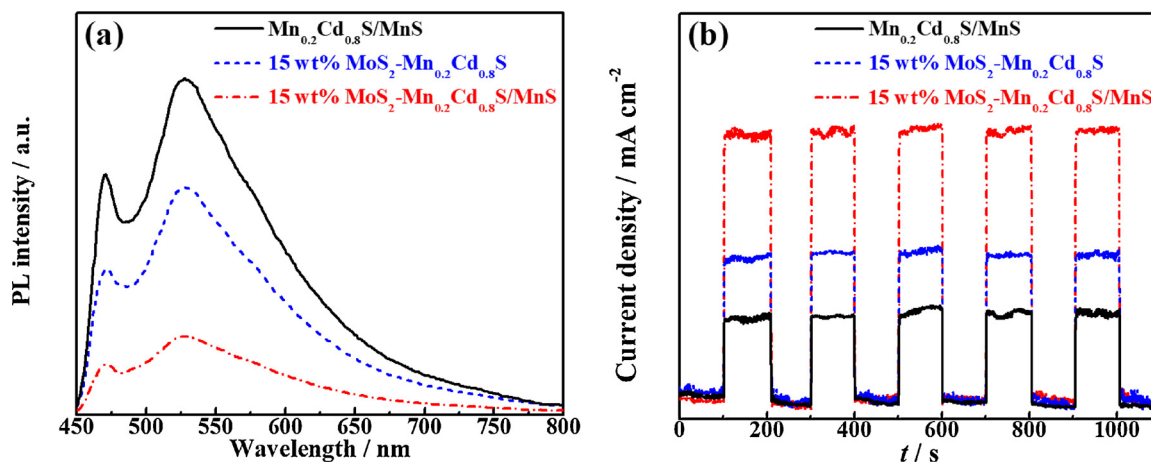


Fig. 10. (a) Photoluminescence (PL) spectra of 15 wt% $\text{MoS}_2\text{-Mn}_{0.2}\text{Cd}_{0.8}\text{S}/\text{MnS}$, $\text{Mn}_{0.2}\text{Cd}_{0.8}\text{S}/\text{MnS}$ and 15 wt% $\text{MoS}_2\text{-Mn}_{0.2}\text{Cd}_{0.8}\text{S}$ with excitation wavelength of 426 nm; (b) Photocurrent-time curves of 15 wt% $\text{MoS}_2\text{-Mn}_{0.2}\text{Cd}_{0.8}\text{S}/\text{MnS}$, $\text{Mn}_{0.2}\text{Cd}_{0.8}\text{S}/\text{MnS}$ and 15 wt% $\text{MoS}_2\text{-Mn}_{0.2}\text{Cd}_{0.8}\text{S}$ under $\lambda \geq 420$ nm light irradiation.

photoinduced electron transfer from the nanoparticle-like α -MnS to the nanorod-like $\text{Mn}_{0.2}\text{Cd}_{0.8}\text{S}$ and then to the nanoflake-like MoS_2 , thus promoting the charge separation and providing more active sites for H_2 production reaction. This study not only presents a novel $\text{Mn}_{0.2}\text{Cd}_{0.8}\text{S}/\text{MnS}$ heterojunction photocatalyst consisting of $\text{Mn}_{0.2}\text{Cd}_{0.8}\text{S}$ solid solution and α -MnS, but also reveals that low cost MoS_2 can replace noble metal Pt as a highly efficient cocatalyst for photocatalytic H_2 production.

Acknowledgments

This work was supported by the Natural Science Foundation of China (21573166 and 21271146), the Funds for Creative Research Groups of Hubei Province (2014CFA007), and the Natural Science Foundation of Jiangsu Province (BK20151247), China.

Appendix A. Supplementary data

Supplementary material related to this article can be found, in the online version, at doi:<https://doi.org/10.1016/j.apcatb.2018.09.033>.

References

- [1] A. Fujishima, K. Honda, *Nature* 238 (1972) 37–38.
- [2] A. Kudo, Y. Miseki, *Chem. Soc. Rev.* 38 (2009) 253–278.
- [3] J.R. Ran, J. Zhang, J.G. Yu, M. Jaroniec, S.Z. Qiao, *Chem. Soc. Rev.* 43 (2014) 7787–7812.
- [4] X.H. Zhang, T.Y. Peng, S.S. Song, J. Mater. Chem. A 4 (2016) 2365–2402.
- [5] M.S. Zhu, X.Y. Cai, M. Fujitsuka, J.Y. Zhang, T. Majima, *Angew. Chem. Int. Ed.* 56 (2017) 7693–7696.
- [6] M.S. Zhu, S. Kim, L. Mao, M. Fujitsuka, J.Y. Zhang, X.C. Wang, T. Majima, *J. Am. Chem. Soc.* 139 (2017) 13234–13242.
- [7] B. Tian, B.N. Tian, B. Smith, M.C. Scott, R.N. Hua, Q. Lei, Y. Tian, *Nat. Commun.* 9 (2018) 1397.
- [8] X.H. Zhang, L.J. Yu, C.S. Zhuang, T.Y. Peng, R.J. Li, X.G. Li, *ACS Catal.* 4 (2014) 162–170.
- [9] J.M. Wang, Y. Zheng, T.Y. Peng, J. Zhang, R.J. Li, *ACS Sustain. Chem. Eng.* 5 (2017) 7549–7556.
- [10] K. Zhang, L.J. Guo, *Catal. Sci. Technol.* 3 (2013) 1672–1690.
- [11] X.J. Zhang, Y.C. Guo, J. Tian, B.T. Sun, Z.Q. Liang, X.S. Xu, H.Z. Cui, *Appl. Catal. B* 232 (2018) 355–364.
- [12] S.S. Song, Z.C. Liang, W.L. Fu, T.Y. Peng, *ACS Appl. Mater. Interfaces* 9 (2017) 17013–17023.
- [13] K. Li, B. Chai, T.Y. Peng, J. Mao, L. Zan, *ACS Catal.* 3 (2013) 170–177.
- [14] X. Jia, M. Tahir, L. Pan, Z.F. Huang, X.W. Zhang, L. Wang, J.J. Zou, *Appl. Catal. B* 198 (2016) 154–161.
- [15] T.Y. Peng, K. Li, P. Zeng, Q.G. Zhang, X.G. Zhang, *J. Phys. Chem. C* 116 (2012) 22720–22726.
- [16] H. Yan, J. Yang, G. Ma, G. Wu, X. Zong, Z. Lei, J. Shi, C. Li, *J. Catal.* 266 (2009) 165–168.
- [17] J. Li, J.H. Yang, F.Y. Wen, C. Li, *Chem. Commun.* 47 (2011) 7080–7082.
- [18] T.Y. Peng, X.H. Zhang, P. Zeng, K. Li, X.G. Zhang, X.G. Li, *J. Catal.* 303 (2013) 156–163.
- [19] Y.B. Wang, J.C. Wu, J.W. Zheng, R. Xu, *Catal. Sci. Technol.* 1 (2011) 940–947.
- [20] Y.G. Chen, S. Zhao, X. Wang, Q. Peng, R. Lin, Y. Wang, R.G. Shen, X. Cao, L.B. Zhang, G. Zhou, J. Li, A.D. Xia, Y.D. Li, *J. Am. Chem. Soc.* 138 (2016) 4286–4289.
- [21] X.J. Liu, P. Zeng, T.Y. Peng, X.H. Zhang, K.J. Deng, *Int. J. Hydrogen Energy* 37 (2012) 1375–1384.
- [22] J.Y. Liu, C.S. Zhuang, K. Li, T.Y. Peng, *Phys. Chem. Chem. Phys.* 17 (2015) 10944–10952.
- [23] L. Ren, F. Yang, Y.R. Deng, N.N. Yan, S. Huang, D. Lei, Q. Sun, Y. Yu, *Int. J. Hydrogen Energy* 35 (2010) 3297–3305.
- [24] J.C. Wu, J.W. Zheng, P. Wu, R. Xu, *J. Phys. Chem. C* 115 (2011) 5675–5682.
- [25] K. Ikeue, S. Shiiba, M. Machida, *Chem. Mater.* 22 (2010) 743–745.
- [26] M.C. Liu, Y.C. Du, L.J. Ma, D.W. Jing, L.J. Guo, *Int. J. Hydrogen Energy* 37 (2012) 730–736.
- [27] M.Y. Liu, L.Q. Zhang, X.X. He, B. Zhang, H.F. Song, S.N. Li, W.S. You, *J. Mater. Chem. A* 2 (2014) 4619–4626.
- [28] H. Liu, J.C. Meng, J. Zhang, *Catal. Sci. Technol.* 7 (2017) 3802–3811.
- [29] K. Ikeue, Y. Shinmura, M. Machida, *Appl. Catal. B* 123 (2012) 84–88.
- [30] H. Liu, Z.Z. Xu, Z. Zhang, D. Ao, *Appl. Catal. A* 518 (2016) 150–157.
- [31] X.L. Liu, X.Z. Liang, P. Wang, B.B. Huang, X.Y. Qin, X.Y. Zhang, Y. Dai, *Appl. Catal. B* 203 (2017) 282–288.
- [32] H.S. Zhai, X.L. Liu, P. Wang, B.B. Huang, Q.Q. Zhang, *Appl. Surf. Sci.* 430 (2018) 515–522.
- [33] X.L. Liu, Q. Liu, P. Wang, Y.Z. Liu, B.B. Huang, E.A. Rozhkova, Q.Q. Zhang, Z.Y. Wang, Y. Dai, J. Lu, *Chem. Eng. J.* 337 (2018) 480–487.
- [34] Q.Z. Huang, Y. Xiong, Q. Zhang, H.C. Yao, Z.J. Li, *Appl. Catal. B* 209 (2017) 514–522.
- [35] X. Zong, H.J. Yan, D.P. Wu, G.J. Ma, F.Y. Wen, L. Wang, C. Li, *J. Am. Chem. Soc.* 130 (2008) 7176–7177.
- [36] Y. Hou, A.B. Laursen, J. Zhang, G. Zhang, Y. Zhu, X. Wang, S. Dahl, *Angew. Chem., Int. Ed.* 52 (2013) 3621–3625.
- [37] Q.J. Xiang, J.G. Yu, M. Jaroniec, *J. Am. Chem. Soc.* 134 (2012) 6575–6578.
- [38] S.S. Song, J.M. Wang, T.Y. Peng, W.L. Fu, L. Zan, *Appl. Catal. B* 228 (2018) 39–46.
- [39] W.J. Jiang, Y.F. Liu, R.L. Zong, Z.P. Li, W.Q. Yao, Y.F. Zhu, *J. Mater. Chem. A* 3 (2015) 18406–18412.
- [40] X.L. Yin, L.L. Li, W.J. Jiang, Y. Zhang, X. Zhang, L.J. Wan, J.S. Hu, *ACS Appl. Mater. Interfaces* 8 (2016) 15258–15266.
- [41] D.P. Kumar, S. Hong, D.A. Reddy, T.K. Kim, *J. Mater. Chem. A* 4 (2016) 18551–18558.
- [42] X.L. Yin, G.Y. He, B. Sun, W.J. Jiang, D.J. Xue, A.D. Xia, L.J. Wan, J.S. Hu, *Nano Energy* 28 (2016) 319–329.
- [43] Z. Lv, N. Mahmood, M. Tahir, L. Pan, X.W. Zhang, J.J. Zou, *Nanoscale* 8 (2016) 18250–18269.
- [44] S. Ma, J. Xie, J.Q. Wen, K.L. He, X. Li, W. Liu, X.C. Zhang, *Appl. Surf. Sci.* 391 (2017) 580–591.
- [45] A.P. Wu, C.G. Tian, Y.Q. Jiao, Q. Yan, G.Y. Yang, H.G. Fu, *Appl. Catal. B* 203 (2017) 955–963.
- [46] X. Zhou, D. Liu, H.L. Bu, L.L. Deng, H.M. Liu, P. Yuan, P.X. Du, H.Z. Song, *Solid Earth Sci.* 3 (2018) 16–29.
- [47] P. Dalvand, M.R. Mohammadi, D.J. Fray, *Mater. Lett.* 65 (2011) 1291–1294.
- [48] J. Yang, J.H. Zeng, S.H. Yu, L. Yang, G.E. Zhou, Y.T. Qian, *Chem. Mater.* 12 (2000) 3259–3263.
- [49] S. Cao, C.J. Wang, X.J. Lv, Y. Chen, W.F. Fu, *Appl. Catal. B* 162 (2015) 381–391.
- [50] B. Hinnemann, P.G. Moses, J. Bonde, K.P. Jørgensen, J.H. Nielsen, S. Hørch, I. Chorkendorff, J.K. Nørskov, *J. Am. Chem. Soc.* 127 (2005) 5308–5309.
- [51] M. Dan, Q. Zhang, S. Yu, A. Prakash, Y.H. Lin, Y. Zhou, *Appl. Catal. B* 217 (2017) 530–539.
- [52] X. Chen, D. Cummins, B.N. Reinecke, E. Clark, M.K. Sunkara, T.F. Jaramillo, *Nano Lett.* 11 (2011) 4168–4175.
- [53] Z. Luo, R. Miao, T.D. Huan, I.M. Mosa, A.S. Poyraz, W. Zhong, J.E. Cloud, D.A. Kriz, S. Thanneeru, J. He, Y. Zhang, R. Ramprasad, S.L. Suib, *Adv. Energy Mater.* 6 (2016) 1600528–1600539.
- [54] W.L. Fu, J.M. Wang, S.Y. Zhou, R.J. Li, T.Y. Peng, *ACS Appl. Nano Mater.* 1 (2018) 2923–2933.
- [55] L.D. Li, J.Q. Yan, T. Wang, Z.J. Zhao, J. Zhang, J.L. Gong, N.J. Guan, *Nat. Commun.* 6 (2015) 5881.
- [56] S.P. Ding, X.Y. Xiong, X.F. Liu, Y.Q. Shi, Q.Q. Jiang, J.C. Hu, *Catal. Sci. Technol.* 7 (2017) 3791–3801.